Intra- and Interhemispheric Signatures of Criticality at the Onset of Synchronization

Leonardo Dalla Porta [1,*,†], Pietro Bozzo [2], Marco N. Pompili [2], Damien Depannemaecker [2], Antonio J. Fontenele [3], Tomoki Fukai [4], Pierpaolo Sorrentino [2,5] and Giovanni Rabuffo [6,*,‡]

[1] *Institute of Biomedical Research August Pi i Sunyer (IDIBAPS), Barcelona, Spain*
[2] *Systems Neuroscience Institute, Aix-Marseille University, Marseille, France*
[3] *Department of Physics, University of Arkansas, Fayetteville, Arkansas, USA*
[4] *Neural Coding and Brain Computing Unit, Okinawa Institute of Science and Technology, Okinawa, Japan*
[5] *Institute of Applied Sciences and Intelligent Systems, National Research Council, Pozzuoli, Italy*
[6] *Center for Brain and Cognition, Pompeu Fabra University, Barcelona, Spain*

(Received 17 December 2025; accepted 16 October 2026; published 17 November 2026)

The cerebral cortex must flexibly alternate between locally segregated activity that supports specialization and long-range interactions that enable integration. How cortical networks balance these competing demands remains unclear. We propose that fluctuations around a critical point between ordered and disordered phases provide a natural framework to understand coordinated neuronal activity across scales. Using simultaneous spiking recordings from the left and right prefrontal cortex of freely behaving rats, we find that signatures of criticality emerge at the onset of neuronal synchronization, both locally within individual hemispheres and globally across the combined population. Over time, cortical activity spans a continuum of intra- and interhemispheric synchrony, including states in which neurons are locally desynchronized yet maintain functional interhemispheric coordination. A computational model operating near its critical regime reproduces these empirical results. When slow fluctuations in local excitability are introduced, the model generates dynamic, activity-dependent interpopulation correlations despite fixed coupling between populations. These results suggest that cortical networks achieve flexible transitions between local and global computation by fluctuating around a critical regime.

DOI: 10.1103/tr2q-757y

I. INTRODUCTION

Cortical organization supports both specialized local processing and coordinated communication across distant regions [1–4]. However, how the brain flexibly balances these competing demands remains a central question in systems neuroscience. In this context, brain criticality offers a theoretical framework to understand how such integration-segregation balance might be achieved in cortical networks [5]. Specifically, this framework proposes that neuronal populations operate near a critical point between order and disorder, where neuronal avalanches are observed across orders of magnitude [6], from local circuits to large-scale activations [7]. These characteristic dynamics maximize information processing [8], and can potentially explain how the brain coordinates local and global communication. Although evidence for brain criticality, at the neuronal scale, has come largely from single-area recordings [9], far less is known about how critical dynamics extend across multiple, interacting brain regions. This gap limits our understanding of whether criticality is a local property of neural circuits, a global feature of distributed networks, or rather a multiscale phenomenon that emerges from their interaction.

Recent work on high-density single-unit recordings revealed that signatures of criticality are not universal across the brain: they may depend on the neuronal subset examined [10,11], the dimensions of activity space analyzed [12,13], or the timescale of observations [14,15]. Collectively, these findings suggest that criticality is not a static regime of brain activity, but a dynamic, context-dependent, and potentially region-specific feature. Key open questions remain: how do the critical dynamics unfold within and between widely separated populations? Do spatially distant areas approach the critical point simultaneously, or can they tune independently? Is criticality preserved when distant populations are considered as a single global system rather than as isolated local circuits?

To address these questions, we recorded spiking activity simultaneously from the left and right prefrontal cortex (PFC) of freely behaving rats [Fig. 1(a)]. This bilateral approach enabled us to track local dynamics within each hemisphere while also assessing the dynamics between them. By measuring population synchrony, neuronal avalanches, and interhemispheric correlations, we aimed to determine whether criticality arose independently in each region, emerged only when populations were considered together, or depended on interactions between them. This approach provided a direct

*These authors contributed equally to this work.
†Contact author: dallaporta@recerca.clinic.cat
‡Contact author: giovanni.rabuffo@upf.edu

Published by the American Physical Society under the terms of the Creative Commons Attribution 4.0 International license. Further distribution of this work must maintain attribution to the author(s) and the published article's title, journal citation, and DOI.

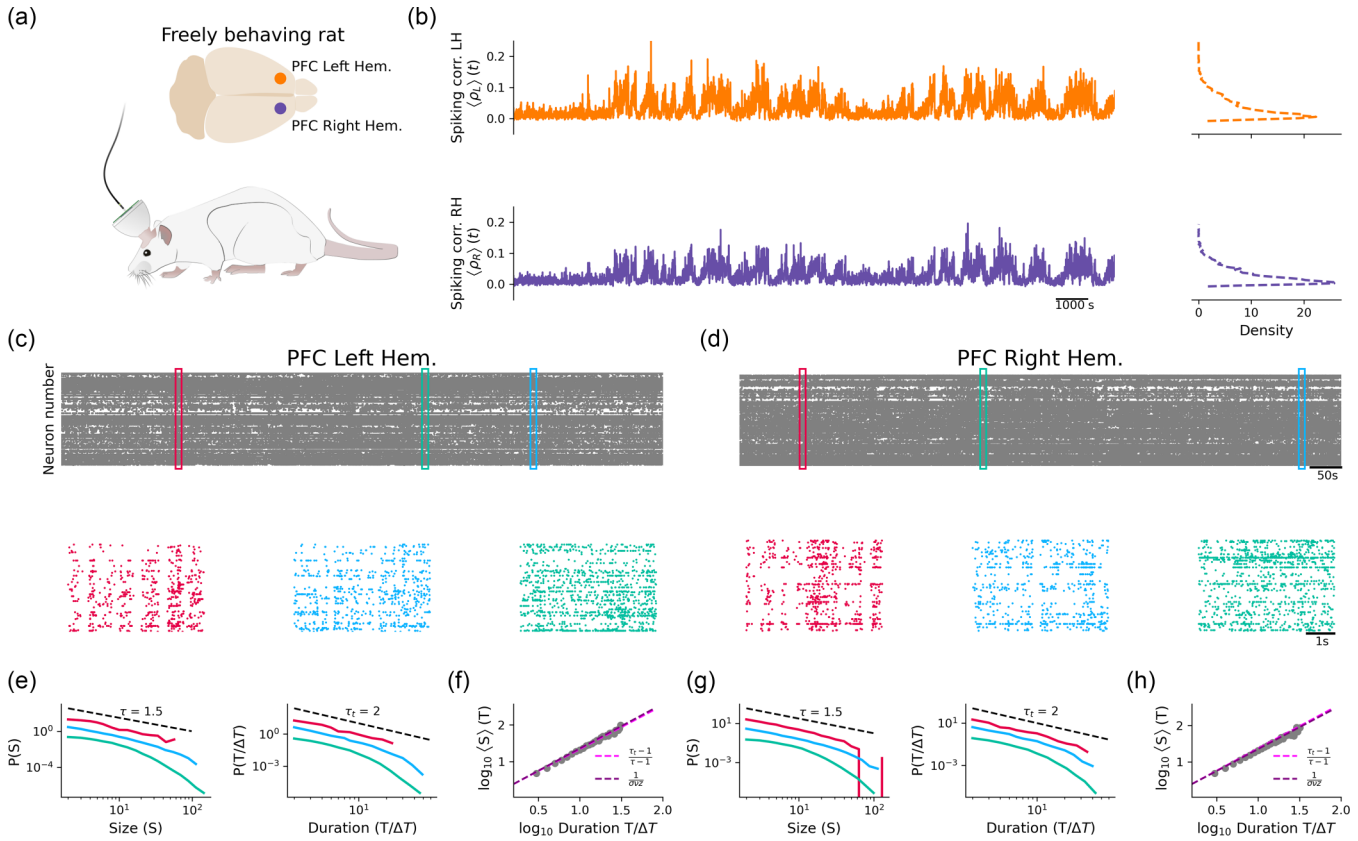


FIG. 1. Signatures of criticality at the onset of synchronization in the freely behaving rat brain. (a) Schematics of the experiment: spiking recordings were performed simultaneously in both hemispheres of the prefrontal cortex (PFC) in freely behaving rats. (b) (Left) Mean intrahemispheric pairwise spiking correlation for left $[\langle\rho_L\rangle(t)]$ and right $[\langle\rho_R\rangle(t)]$ PFC regions, computed over 5-s nonoverlapping time windows. (Right) $\langle\rho\rangle(t)$ histograms. (c) (Top) Raster plot of the spiking activity throughout the session. (Bottom) Zoomed-in raster plot illustrating the spiking activity dynamics for different levels of synchrony: high ($\langle\rho\rangle \simeq 0.18$; red), intermediate ($\langle\rho\rangle \simeq 0.09$; blue), and low ($\langle\rho\rangle \simeq 0.02$; green). (d) Same as in (c) but for the right PFC region. (e), (g) Neuronal avalanche distributions for size $[P(S) \sim S^{-\tau}]$ and duration $[P(T) \sim T^{-\tau_t}]$ in the left (e) and right (g) PFC regions. The exponents obtained for the left (right) PFC regions during intermediate levels of synchrony are $\tau = 1.72$ ($\tau = 1.65$) and $\tau_t = 1.85$ ($\tau_t = 1.78$). Power-law fit and exponent estimation are performed using a maximum likelihood estimator, as described in [16], setting a lower and upper bound for size ($x_{\min} = 3$, $x_{\max} = 35$) and duration ($x_{\min} = 2$, $x_{\max} = 18$). The Akaike information criterion confirms that the data are better described by a power-law distribution than by a log-normal distribution (Fig. S3 in the Supplemental Material [17]). Dashed lines represent the original exponents reported in [6], which coincide with those of the mean-field directed percolation universality class [18]. The colors correspond to the states described in (c). (f), (h) Neuronal avalanches for size and duration at intermediate levels of synchrony follow the scaling relation predicted at criticality $\frac{1}{\nu\sigma z} = \frac{\tau_t - 1}{\tau - 1}$ [19]. The first term (pink dashed line) is fitted from the empirical data where $\frac{1}{\nu\sigma z} = 1.21$ and $\frac{1}{\nu\sigma z} = 1.20$ for the left (f) and right (h) regions, respectively. The second term (purple dashed line) is predicted by the relationship between avalanche exponents obtained in (e) and (g). Data shown is from one representative rat session.

way to link local fluctuations in synchrony with large-scale coordination and to test how long-range coupling shaped the expression of critical dynamics across the cortex. Finally, we used a mesoscale computational model with a known critical point to test whether the multiscale coordination observed experimentally is an intrinsic feature of networks fluctuating near criticality.

II. RESULTS

A. Critical neuronal avalanches at the onset of synchronization

We simultaneously recorded spiking activity from hundreds of neurons from the left and right prefrontal cortex (PFC) in freely behaving rats [n=3; Fig. 1(a)]. Each recording session lasted approximately 8 h (n_s=2 sessions per rat), yielding a total of 620 neurons (single-unit activity, SUA): 334 neurons in the left PFC and 286 neurons in the right PFC. To quantify the level of synchrony, we computed the mean pairwise spiking correlation, $\langle\rho\rangle$, in nonoverlapping 5-s windows, following the same approach as in [16]. Here, the underlying assumption is that neuronal dynamics do not *rigidly* operate at a critical point; rather, they hover around a critical point, fluctuating between phases of order and disorder [16,21–24].

By evaluating cortical dynamics independently in the left and right PFC populations, we observed that local population activity spontaneously alternated between periods of high and low synchrony, reflecting more ordered and more disordered states, respectively [Fig. 1(b)]. High-synchrony periods were characterized by synchronous bursts of neuronal activations [Figs. 1(c) and 1(d), red], whereas low-synchrony periods

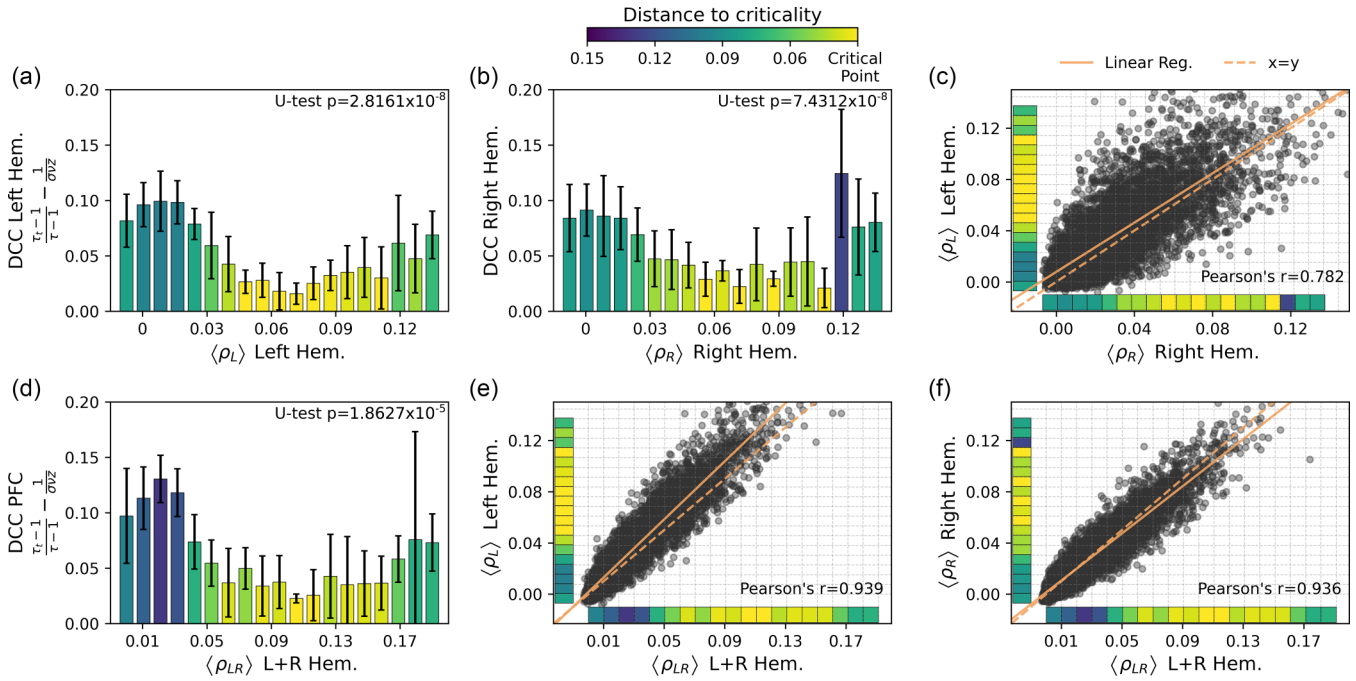


FIG. 2. Distance to criticality coefficient (DCC) indicates the proximity to a critical region at the edge of synchrony. (a), (b) DCC as a function of the population synchrony level, defined as the mean pairwise spiking correlation ($\langle\rho\rangle$), for the left ($\langle\rho_L\rangle$) and right ($\langle\rho_R\rangle$) hemisphere populations, respectively. Bar colors indicate the distance to criticality according to the color scale shown, with lower DCC values corresponding to points closer to the critical regime. The reported p-value corresponds to the test for a U-shaped relationship [20] between DCC and synchrony by requiring the slope of a fitted quadratic to be significantly negative at the lower bound and significantly positive at the upper bound of the observed range (see Sec. IV). (c) Scatter plot of $\langle\rho\rangle(t)$ for the left vs right hemispheres. Each point represents one 5-s time window. Marginal color bars show the corresponding DCC values across synchrony bins for each hemisphere, as in (a), (b). (d) DCC as a function of $\langle\rho\rangle$ for the merged left and right PFC populations ($\langle\rho_{LR}\rangle$). Bar colors indicate distance to criticality as in (a), (b). (e), (f) Scatter plots of the merged population $[\langle\rho_{LR}\rangle(t)]$ vs the left (e) and right (f) populations, respectively. Marginal color bars indicate the DCC values across synchrony bins for the corresponding local and merged populations. In (c), (e), (f) the solid orange line indicates linear regression, the dashed orange line indicates the identity line ($x = y$), and Pearson's correlation coefficient is reported. Data in (c), (e), (f) are from one representative rat session, the same as used in Fig. 1.

exhibited irregular firing patterns [Figs. 1(c) and 1(d), green]. Intermediate levels of synchrony were also observed [Fig. 1(c) and 1(d), blue], during which the dynamics displayed complex spatiotemporal activity patterns known as neuronal avalanches [6]. Following the original definition [6] and the methodology of [16,25], we defined the size of an avalanche as the sum of spiking activity in consecutive occupied time bins (ΔT), with ΔT being computed for each 5-s segment as the mean interspike interval of the pooled population spike train. Avalanche duration was determined by the number of consecutive active time bins. Avalanches were computed separately within each 5-s window and grouped according to the population synchrony level ($\langle\rho\rangle$) using 30 nonoverlapping bins spanning the full observed range of $\langle\rho\rangle$.

Analyzing neuronal avalanches independently for each PFC population revealed that, at intermediate levels of synchrony, both the size [$P(S) \sim S^{-\tau}$] and duration [$P(T) \sim T^{-\tau_t}$] of events were well described by a power-law distribution, a hallmark signature of critical dynamics [6,26] (Figs. 1(e)–1(g), SM Figs. S1 and S2 [17]). Consistent with this result, direct model comparison using the Akaike information criterion (AIC) showed greater relative support for the power-law model than for the log-normal model for both avalanche size and duration (SM Fig. S3 [17]). Moreover, the scaling relation $\frac{1}{\sigma\nu_z} = \frac{\tau_t - 1}{\tau - 1}$, expected to hold at criticality, was also satisfied [19] [Figs. 1(f)–1(h)]. Here, the first term was obtained empirically by fitting $\langle S\rangle(T) \sim T^{\frac{1}{\nu\sigma z}}$ to the neuronal avalanches [Figs. 1(f)–1(h)], while the second term was estimated from the fitted avalanche exponents τ and τ_t [19,27]. This scaling relation has been used in the literature as a stringent test of criticality [16,19,21], with the absolute difference between the left- and right-hand terms defined as the "distance to criticality coefficient" (DCC) [21].

Evaluating the DCC across synchrony levels revealed a nonmonotonic dependence between population synchrony and proximity to criticality. In both hemispheres, DCC reached its lowest values at intermediate synchrony levels, indicating that agreement with the crackling-noise scaling relation was strongest at the onset of synchronization [Figs. 2(a) and 2(b)]. This pattern persisted when larger time windows were used (SM Fig. S4 [17]). For all cases, we applied a test for a U-shaped relationship [20] and found statistically significant evidence for such a relationship (Fig. 2 and SM Fig. S4 [17]). Accordingly, the local PFC dynamics were closest to the critical regime, not during fully desynchronized or highly synchronized activity, but in an intermediate state between disorder and order. At high levels of synchrony ($\langle\rho\rangle \gtrsim 0.15$),

a less frequently occupied state [see histogram in Fig. 1(b)], DCC was often undefined because the dynamics were dominated by a few large avalanches.

Thus our analysis showed that each PFC population approached the critical regime at intermediate levels of synchronization. We refer to this as *local criticality*, because the analysis was performed independently in the left and right populations. This finding aligns with previous theoretical work, where critical neuronal avalanches have been described at the edge of synchrony [24,28,29]. However, it is not yet known whether local critical fluctuations align across distant regions. Put differently, when examined within the same time window, do left and right PFC populations converge on the same near-critical state, or can they reside in distinct, and potentially opposite, regimes such as subcritical versus supercritical?

B. Asymmetric relationship between local and global criticality

To evaluate the dynamic relationship between distant populations, we compared $\langle \rho_{L,R} \rangle(t)$ of the left and right PFC within each time window. As illustrated in Fig. 1(b), the synchronization profiles of the left and right PFC closely tracked each other [27–30]. In particular, we observed that intermediate levels of synchrony typically occurred simultaneously in both populations [Pearson's $r = 0.782$; Fig. 2(c)]. Nonetheless, at certain times, one population appeared to be closer to the critical state than the other. These observations are consistent with evidence that, despite the structural similarities between homotopic regions, the functional operations of the left and right PFC may diverge at certain times [31–33].

To determine whether the apparent coordination between distant populations could arise by chance, we generated 1000 surrogate datasets by shuffling $\langle \rho_R \rangle(t)$ time series (one value per time window), thereby preserving intrapopulation correlations while disrupting interpopulation correlations. By comparing the occupancy probabilities across synchronization bins, we found that the empirical data exhibited significantly more co-occurrence of matching states than any of the surrogates (SM Fig. S5 [17]). Thus the observed interhemispheric coordination reflects structured temporal alignment between hemispheres rather than a statistical coincidence under this surrogate procedure.

These observations raise the question of whether critical dynamics emerge not only locally within each hemisphere but also globally when both populations are considered as one. To address this, we repeated the same analysis, merging the left and right PFC into a single population, referred to as L + R. DCC analysis showed that criticality was again more pronounced at intermediate levels of synchrony [Fig. 2(d)], consistent with the results obtained when analyzing the regions separately [Figs. 2(a) and 2(b)]. We refer to this as *global criticality*, because the analysis was performed by merging both the left and right populations. This finding raised a further question: does global criticality require simultaneous criticality in each hemisphere, or can it emerge independently of the local states?

To address this question, we compared the synchrony of the left and right PFC populations, $\langle \rho_{L,R} \rangle(t)$, with that of the merged population, $\langle \rho_{LR} \rangle(t)$. We observed instances in which the distance to criticality was reduced at the global level, i.e., in the merged population, without a corresponding reduction in either hemisphere individually [Figs. 2(e) and 2(f)]. Conversely, there were moments when one or both hemispheres independently exhibited a closer proximity to critical dynamics, whereas the merged population did not [Figs. 2(e) and 2(f)]. These results indicate that local, within-population, and global, merged-population, signatures of criticality do not always coincide, highlighting the complex coordination of critical dynamics across scales.

C. Intra- and interhemispheric correlations exhibit structured coordination

Large-scale brain studies have shown that cortical regions participate in long-range interactions across the connectome, alternating between integrated and segregated phases [4,30,34–39]. Here, we hypothesized that similar long-range interactions might underlie the fluctuations in neuronal population dynamics observed in our recordings, including the fluctuations around criticality (Figs. 1 and 2). To quantify these interactions, and as a proxy of integration [40], we computed interhemispheric correlations between neurons in the two PFC regions, excluding intrahemispheric correlations (Fig. 3). Therefore, time windows with low interhemispheric correlation were considered segregated states, whereas those with high values reflected integrated activity across populations.

We found that interhemispheric correlations followed a smooth, nontrivial gradient that depended on the intrahemispheric correlation levels within the left and right PFC (Fig. 3(a), left; SM Fig. S6 [17]). In other words, epochs with stronger intrahemispheric correlations were associated with higher interhemispheric correlations. To determine whether this gradient could arise trivially from increased synchronous events, we generated 1000 surrogate datasets by randomly permuting time bins within each 5-s epoch independently for the two populations. This preserved intrahemispheric correlations while disrupting interhemispheric dynamics [Figs. 3(a) and 3(b)]. In the surrogates, both the gradient and the overall magnitude of interhemispheric correlations were disrupted. This confirmed that the empirical dependence requires preserved cross-hemispheric temporal structure and is not explained by independent within-hemisphere synchrony alone.

Hence the resulting gradient [Fig. 3(a), left] indicated that local intrahemispheric synchrony shapes interhemispheric coupling. Specifically, (i) when both hemispheres showed low intrahemispheric correlation, corresponding to a subcritical state, the two regions remained segregated, with minimal interhemispheric correlations [Fig. 3(c), scenario 1]; (ii) when both hemispheres were highly synchronized, corresponding to a supercritical state, they entered an integrated state with high interhemispheric correlations [Fig. 3(c), scenario 5]; and (iii) intermediate levels of interhemispheric correlations, reflecting a balanced state between integration and segregation, occurred when intrahemispheric correlations were intermediate in both regions [Fig. 3(c), scenario 3], i.e., near a critical state, as well as when one region displayed high intrahemispheric correlations while the other remained desynchronized [Fig. 3(c), scenarios 2 and 4]. In particu-

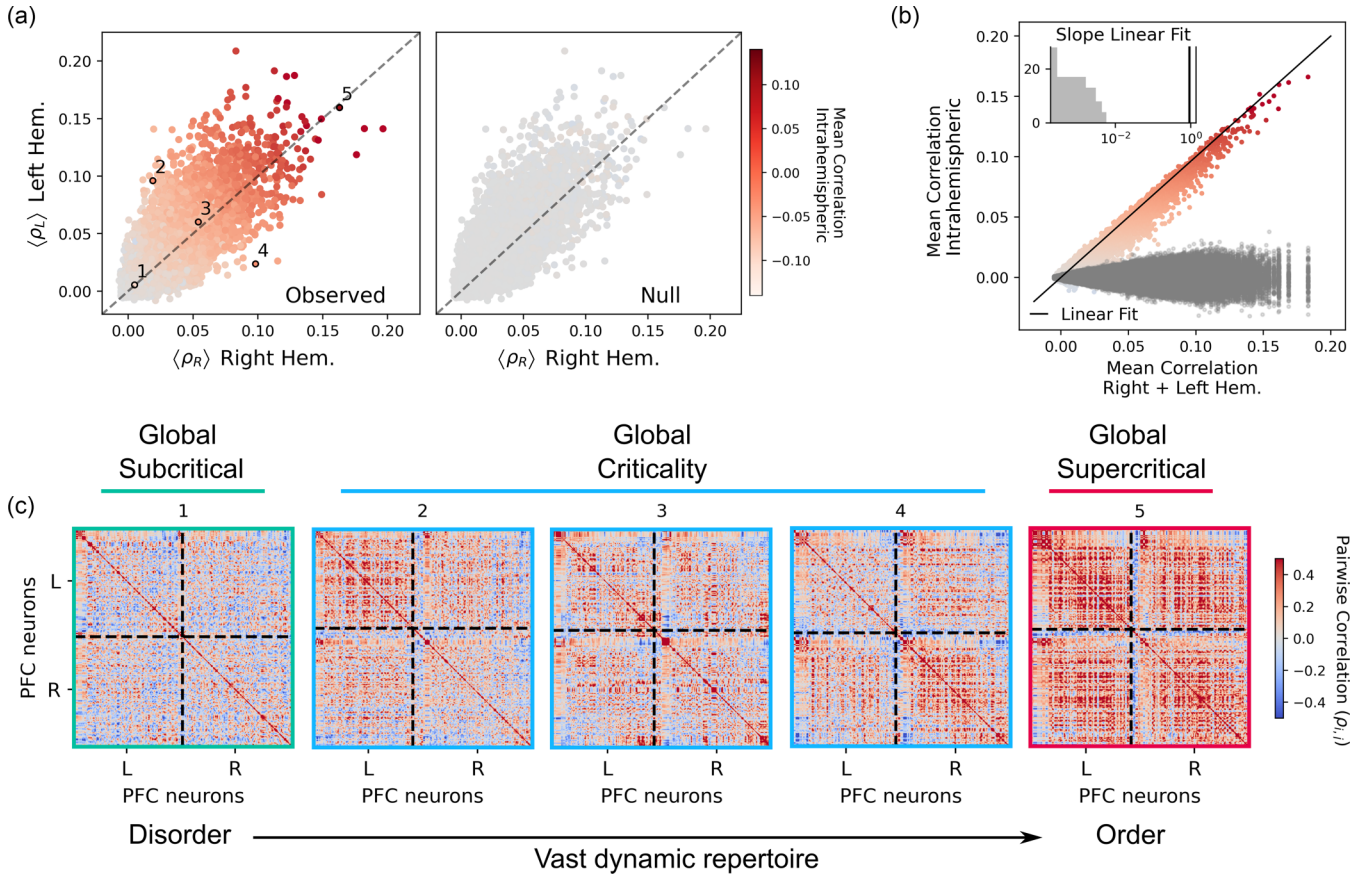


FIG. 3. Interhemispheric correlations depend on the level of intrahemispheric correlations. (a) Scatter plots of intrahemispheric synchrony, measured as mean pairwise correlations within the left ($\langle\rho_L\rangle$) and right ($\langle\rho_R\rangle$) hemisphere populations. Each dot represents a 5-s window, color coded by the magnitude of interhemispheric correlations, excluding intrahemispheric correlations. In the observed data (left), $\langle\rho_L\rangle$ and $\langle\rho_R\rangle$ tend to fluctuate together, with stronger interhemispheric correlations emerging when both are locally synchronized. In the null model (right), generated by shuffling time bins within each epoch independently for the two populations, this structured relationship is abolished. Numbers (1–5) correspond to representative windows shown in (c). (b) Mean interhemispheric correlations increase systematically with mean intrahemispheric correlations (average of left and right populations) in the observed data (colored points). This dependence disappears in the null model (gray points). The inset shows the distribution of slopes obtained from surrogate datasets (gray), demonstrating that the observed slope (black line) lies far outside the null distribution. (c) Representative correlation matrices from the five epochs highlighted in (a). An intrahemispheric correlation value [i.e., the x or y coordinate of a data point in panel (a)] corresponds to the average value of a diagonal block, while an interhemispheric correlation value [i.e., the color scale in panel (a)] corresponds to the mean of the off-diagonal blocks. The five matrices illustrate different scenarios: scenario 1 shows low interhemispheric correlation ($\langle\rho\rangle = 0.0004$) associated with low intrahemispheric correlations; scenarios 2–4 display moderate interhemispheric correlation ($\langle\rho\rangle = 0.045$ for all three), with varying patterns of intrahemispheric correlations: scenario 2 shows higher intrahemispheric correlations in the left hemisphere, scenario 3 shows moderate intrahemispheric correlations distributed evenly across both hemispheres, and scenario 4 shows higher intrahemispheric correlations in the right hemisphere; scenario 5 represents high interhemispheric correlations ($\langle\rho\rangle = 0.139$) accompanied by high intrahemispheric correlations in both hemispheres. Data shown are from one representative rat, the same as used in Fig. 1.

lar, in scenarios 2–4, the interhemispheric correlations (i.e., the average of the off-diagonal block) were nearly the same ($\langle\rho\rangle \simeq 0.045$). Therefore, these findings revealed a nontrivial aspect of cortical dynamics: neurons can exhibit significant interhemispheric correlations (global communication) without requiring high intrahemispheric synchronization (local communication).

D. Specificity of interhemispheric correlations

We showed that intrahemispheric synchrony and interhemispheric coordination exhibit a nontrivial relationship [Fig. 3(a)]. To determine whether this structure was specific to the anatomical left-right organization, rather than a generic consequence of partitioning a correlated population, we performed two complementary controls.

First, we performed a random partition control in which neurons from the left and right PFC were pooled and randomly reassigned into two virtual populations matched in size to the empirical left and right PFC populations. Avalanche size and duration distributions at intermediate synchrony were largely preserved under this control (SM Fig. S7 [17]). This was expected because avalanches were computed within short 5-s windows and then grouped according to synchrony level;

therefore, if the recorded population expresses critical-like dynamics at intermediate synchrony, random subsets of neurons can retain similar avalanche statistics. Thus, in our framework, avalanche scaling alone should not be interpreted as a hemisphere-specific effect (see Discussion).

In contrast, the interpopulation correlation structure was strongly altered by the random partition (SM Fig. S8 [17]). The two virtual populations collapsed more strongly toward the identity line, indicating that their synchrony fluctuations were more redundant than those of the empirical left and right hemispheres (SM Fig. S8 [17], top row). Moreover, the slope of the interpopulation correlation gradient was, in most cases, significantly steeper for the random partitions than for the anatomical left-right split (SM Fig. S8 [17], bottom row). Thus, although arbitrary partitions of the recorded population can preserve local avalanche statistics and generate a synchrony-dependent correlation gradient, they do not reproduce the geometry of the empirical interhemispheric relationship. These results indicate that the structured left-right relationship observed in the data (Fig. 3) is not equivalent to splitting a near-critical population into two arbitrary groups.

Second, we tested whether the observed gradient could be explained by a common slow fluctuation acting on correlated neurons within a single hemisphere. For this control, we repeatedly split neurons from one hemisphere into two virtual populations of the same size and recomputed the correlation gradient between populations. To ensure a matched comparison, we also generated a size-matched empirical distribution by repeatedly subsampling neurons from the real left and right PFC populations and recomputing the left-right gradient. The virtual partitions within the hemisphere produced significantly steeper gradients than the empirical left-right split matched to size (SM Fig. S9 [17]). This indicates that a gradient can arise from shared fluctuations in the local state, but that such partitions yield a more redundant relationship than the empirical interhemispheric organization.

Together, these controls clarify the scope of the bilateral result. Avalanche statistics at intermediate synchrony were robust to subsampling and should not be taken, by themselves, as evidence for a hemispheric-specific effect. In contrast, the anatomical left-right split yielded a correlation structure that differed from both arbitrary partitions of the full recorded population and virtual partitions within a single hemisphere. Given that the recordings came from homotopic PFC regions, shared state fluctuations likely contribute to this coordination. However, the observed geometry was not fully explained by local subsampling alone.

E. A minimal two-population model reproduces the relationship between local synchrony and interpopulation coordination

To test whether a system with a known critical point could account for the correlation structure observed in the data [Fig. 3(a)], we described each population as a network of N all-to-all coupled "active rotator" neurons, parametrized by values for the neurons' intrinsic drive (ω), noise amplitude (σ), and excitability (a) [41,42]. Here, we fixed $\omega = 1$ and $\sigma = 0.499$ as in [41], and used a as the control parameter. As a increased, the mean pairwise spike correlation ($\langle\rho\rangle$) decreased, moving the population from a synchronous regime to an asynchronous regime through an intermediate regime at the edge of synchrony [Fig. 4(a)]. To identify the critical operating point independently, we computed the susceptibility of the population activity, measured as the Fano factor. Susceptibility peaked at the synchronization transition, defining ($a_{\mathrm{crit}} \simeq 1.07$) [Fig. 4(b)]. At this same operating point, the model displayed scale-free avalanche statistics [Fig. 4(c)], consistent with previous results for this active-rotator model [41].

We then extended the model to two coupled populations and quantified how interpopulation coordination depended on the coupling strength, G. Increasing G increased the mean interpopulation correlation [Fig. 4(d)], confirming that G controls the strength of the interaction between populations. We then fixed G and varied the local operating point (determined by a) of each population independently. This produced a smooth gradient in which interpopulation correlation increased with the local synchrony of the two populations [Fig. 4(e)], a pattern that was not reproducible when considering two uncoupled populations, i.e., $G = 0$ (SM Fig. S10 [17]). Importantly, similar levels of interpopulation correlation could arise from different combinations of local dynamical regimes. Thus the model reproduces the empirical observation that long-range coordination depends on local synchrony, while also showing that this relationship is not a simple one-to-one mapping between the local states of the two populations.

F. Slow modulation of local excitability drives fluctuations around criticality

The previous analysis established the static dynamical structure of the model, but the empirical recordings showed that synchrony fluctuates over time. To reproduce this temporal structure, we allowed the control parameter a of each population to vary slowly in time as an Ornstein-Uhlenbeck process centered on a_{crit} (see Methods). This slow drive represents a phenomenological model of state-dependent changes in local excitability, such as those associated with arousal, neuromodulatory tone, behavior, or other slow afferent inputs.

Under this slow modulation, the susceptibility of a representative population fluctuated on a second timescale as the local drive approached or moved away from the critical point [Fig. 5(a)]. Consistently, susceptibility was maximal when $a(t)$ was close to a_{crit} and decreased as the drive moved away from the critical regime [Fig. 5(b)]. In the two-population model, the excitability drives of the two populations were correlated but not identical, allowing coordinated fluctuations around criticality together with transient asymmetric excursions in which the two populations occupied different local regimes [Fig. 5(c)].

Finally, we performed a mechanistic ablation analysis to quantify how different model ingredients contributed to the amplitude of the susceptibility fluctuations. Removing the slow modulation of $a(t)$, by keeping a fixed, reduced the susceptibility fluctuations to the baseline level observed in the absence of a time-varying drive [Fig. 5(d)]. This indicated that slow modulation of local excitability was the main driver of fluctuations around criticality in the model. The remaining ablations showed that shared input, interpopulation coupling,

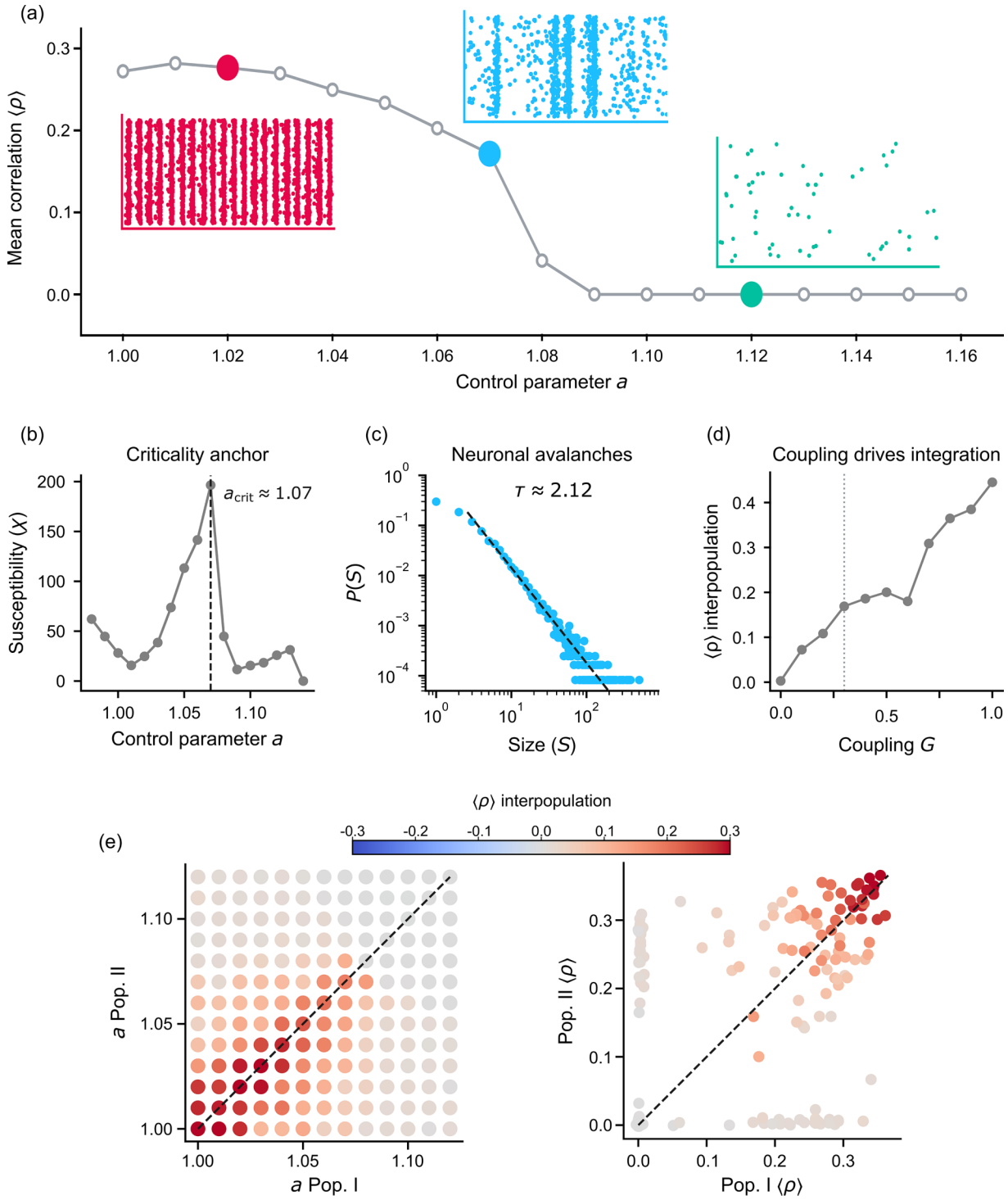


FIG. 4. A computational model reproduces nontrivial intra- and interpopulation correlations. (a) Population synchrony, measured as the mean pairwise correlation $\langle\rho\rangle$ as a function of the control parameter a in the single-population model of [41]. Neurons are coupled all to all, and the control parameter a modulates network excitability. Example raster plots illustrate the synchronous regime (red); the intermediate regime at the model's critical point, $a = 1.07$ (blue); and the asynchronous regime (green). Two hundred fifty neurons are shown during 500 ms. (b) Susceptibility (χ), measured as the Fano factor of population activity, as a function of the control parameter a. Susceptibility is maximal at the critical point. (c) At the critical point, neuronal avalanches follow a power-law distribution, as previously reported in [41]. (d) Mean interpopulation (interhemispheric) correlation as a function of the interpopulation coupling strength G. The dashed vertical line marks the value used in the remaining two-population simulations ($G = 0.3$). (e) (Left) Interpopulation correlations obtained by simulating two weakly coupled populations (Pop. I and Pop. II) varying the control parameter a. Color code indicates the magnitude of the mean interpopulation pairwise correlations. (e) (Right) Scatter plot of intrapopulation synchrony within population I (Pop. I $\langle\rho\rangle$) and population II (Pop. II $\langle\rho\rangle$). Each point corresponds to one pair ($a_{\text{Pop.I}}$, $a_{\text{Pop.II}}$), color coded by the interpopulation correlations magnitude. Dashed line illustrates where $a_{\text{Pop.I}} = a_{\text{Pop.II}}$.

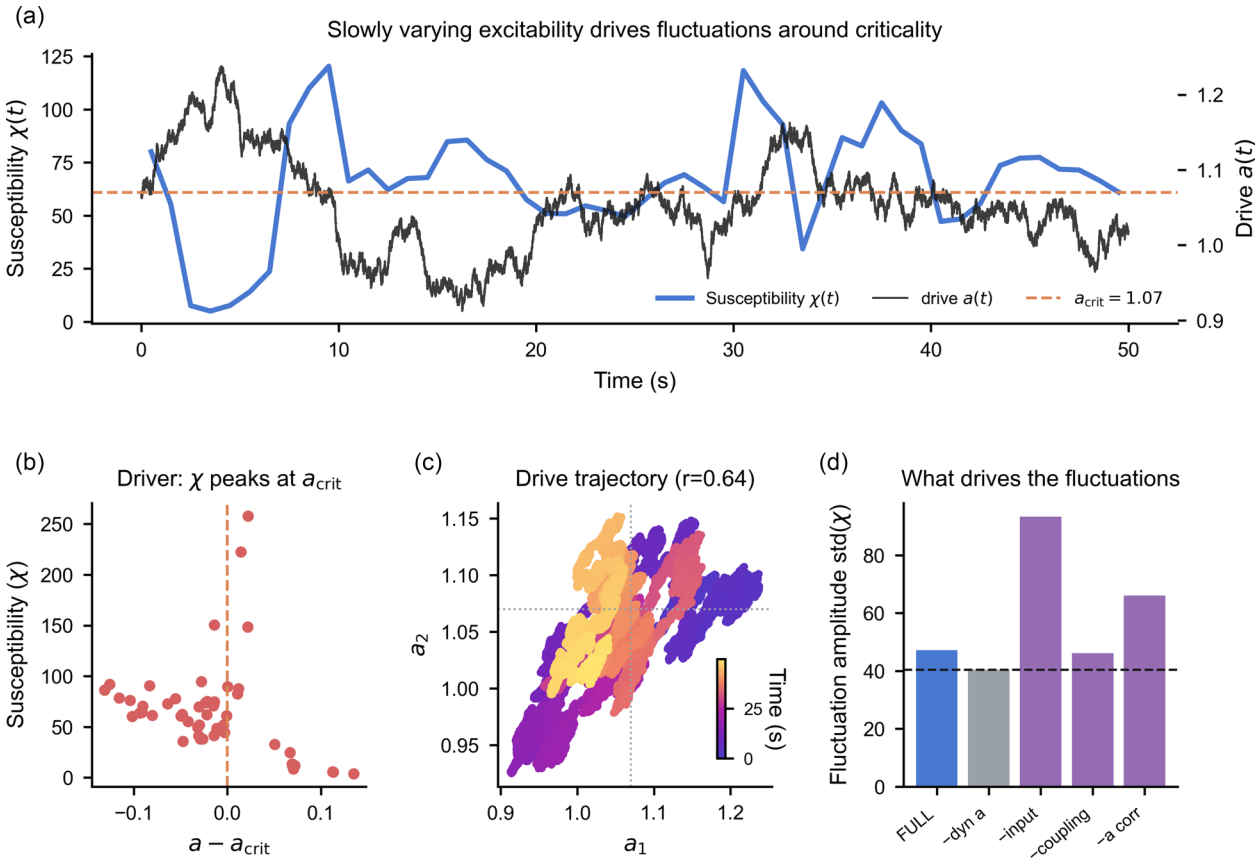


FIG. 5. Slow modulation of local excitability drives fluctuations around criticality. (a) Susceptibility (χ), measured as the Fano factor of the population activity, over time for one representative population in the coupled two-population model. Slow fluctuations were modeled by allowing the control parameter a to vary over time as an Ornstein-Uhlenbeck process. The resulting drive [$a(t)$] is shown in black, with amplitude given by the right y axis. Susceptibility was modulated accordingly, rising and falling on a timescale of seconds and reaching maximal values when $a(t)$ approaches the critical point ($a_{\text{crit}} = 1.07$; dashed orange line). (b) Susceptibility as a function of the distance to the critical point, given by the deviation of the local drive from the critical point ($a - a_{\text{crit}}$). Susceptibility was maximal near a_{crit}, illustrating that temporal fluctuations reflect excursions toward and away from the critical regime. (c) Trajectory of $a(t)$, i.e., the time-varying distance to criticality, of the two coupled populations in the (a_1, a_2) plane, colored by time. The slow drive fluctuations are correlated across the two populations but not identical ($r = 0.64$; Sec. IV), allowing coordinated fluctuations around criticality together with asymmetric excursions in which the two populations occupy different local regimes. (d) Mechanistic ablation study quantifying the contribution of each model ingredient to the amplitude of the susceptibility fluctuations. Fluctuation amplitude was measured as [std(χ)] for the full model and after removing individual components: dynamic modulation of the control parameter a (-dyn a), shared input (-input), interpopulation coupling (-coupling), and correlation between the two excitability drives (-a corr). Dashed line marks simulations when the excitability drive was removed, i.e., $a(t) = a$. This ablation study indicates that slow modulation of local excitability is the main driver of fluctuations around criticality, while the remaining ablations quantify how shared input, interpopulation coupling, and correlated drives shape the amplitude of these fluctuations.

and correlations between the two excitability drives modulated the amplitude of these fluctuations, but did not generate them in the absence of the slow local drive. Together, the model suggests that fixed interpopulation coupling can give rise to dynamic functional coordination when local populations fluctuate around a critical operating point.

III. DISCUSSION

Our results demonstrate that critical dynamics in the prefrontal cortex of freely behaving rats depend on the instantaneous level of population synchrony. When examined independently, each hemisphere displayed scale-free avalanche statistics and consistent scaling relations specifically at intermediate synchrony levels (Fig. 1) [19,27]. While high synchrony collapsed avalanche like activity into a few large events, low synchrony produced irregular activity without signatures of criticality. These findings support the view that spontaneous cortical activity fluctuates around a critical regime, rather than *statically* operating at a critical point, and that signatures of criticality are observed at the edge of synchronization [16,24,28,43,44].

A key finding is that local and global distance to criticality do not necessarily align (Fig. 2). When the left and right populations were merged, the combined activity sometimes approached the critical regime, as indicated by lower DCC values, even when neither hemisphere was individually close to this regime. Conversely, one or both hemispheres could approach the critical regime while the merged population remained farther from it. This dissociation

indicates that proximity to criticality does not scale trivially with population size [10]. Instead, it depends on both local population dynamics and interactions between populations, highlighting the multiscale structure of spontaneous cortical activity [45].

Long-range interactions between hemispheres further revealed a structured, nontrivial relationship between local synchrony and interhemispheric coordination (Fig. 3, SM Fig. S6 [17]). Interhemispheric correlations increased smoothly with intrahemispheric synchrony, and intermediate levels of interhemispheric correlations emerged not only when both hemispheres exhibited intermediate synchrony but also when one hemisphere remained desynchronized. This asymmetric configuration indicates that interhemispheric coordination does not require matched internal states, and that cortical populations can maintain cross-regional coordination even when local dynamics differ.

This structure was not reproduced by controls that preserved local population statistics while disrupting different aspects of the bilateral organization. Temporal shuffling within epochs reduced the interhemispheric gradient, indicating that the effect was not explained by local coactivation strength alone (Fig. 3). Random partitions of the recorded population preserved avalanche statistics but collapsed more strongly toward the identity line and showed steeper synchrony-correlation gradients (SM Figs. S7 and S8 [17]). Virtual partitions within a single hemisphere also produced synchrony-dependent gradients, consistent with shared local state fluctuations, but these gradients were more redundant than the empirical left-right relationship (SM Fig. S9 [17]). These comparisons indicate that the empirical interhemispheric structure is not reproduced by arbitrary subsampling or by splitting a single local population. At the same time, they leave open an important mechanistic possibility: because the recordings were obtained from homotopic PFC regions, part of the observed coordination may reflect shared brain-state fluctuations [46,47] rather than direct interhemispheric coupling alone.

To mechanistically explore this possibility, we turned to a dynamical model in which the critical point is known and can be controlled [41]. This was essential because the empirical data only provide indirect access to distance from criticality through avalanche scaling and DCC, whereas the model allows the distance from the transition to be manipulated explicitly (Fig. 4). Weakly coupling two populations and varying the local control parameter a independently was sufficient to reproduce the empirical gradient between local synchrony and interpopulation coordination, showing that the observed relationship can emerge when populations occupy different positions relative to the synchronization transition [Fig. 4(e)]. Therefore, it indicates that the gradient does not require imposing a time-varying functional coupling. It follows from the state dependence of correlations in coupled populations near the transition.

We then asked how such operating points could be visited dynamically. To this end, we introduced a slow modulation of a as a phenomenological representation of state-dependent changes in local excitability, such as those associated with neuromodulatory tone, arousal, or ongoing behavior, variables known to coordinate widespread fluctuations in neuronal activity [46–49]. This slow drive moved each population toward and away from the critical regime, producing fluctuations in susceptibility on a second timescale (Fig. 5). When the drives were correlated but not identical across populations, the model generated coordinated excursions around the critical point while preserving transient asymmetries between local regimes. In this sense, the model provided a bridge between the static correlation structure and the temporal fluctuations observed in the recordings: slow state-dependent modulation can move local populations through the parameter region where the gradient is expressed.

Together, these simulations support an interpretation in which interhemispheric coordination reflects the combined action of local state-dependent modulation and coupling between populations [50–52]. Shared or correlated brain-state fluctuations may tune local populations relative to the critical regime, while interpopulation coupling determines how these local changes are expressed as correlations across regions. This view is consistent with recent work showing that spontaneous behavior and arousal-related variables modulate widespread neuronal activity and suggests a dynamical route by which global state variables can influence both local synchrony and interhemispheric coordination [46,47,49].

Altogether, our results support a multiscale view of criticality in which local synchrony shapes, but does not fully determine, global network behavior. In this view, criticality provides a regime that maximizes flexibility: it enables local populations to explore diverse spatiotemporal patterns while allowing dynamic coupling across regions [Fig. 3(c)], consistent with accounts proposing that networks near a continuous phase transition balance segregation and integration [26,40,53,54].

More broadly, our findings extend neuronal signatures of criticality beyond isolated cortical populations and emphasize critical dynamics as a potential organizing principle for distributed cortical interactions. Regardless, our study also has limitations. For instance, we focused on homotopic PFC regions, which, despite at times exhibiting distinct temporal dynamics, often fluctuated in unison, likely reflecting their shared structural connectivity and computational roles [32,38,50,55]. As large-scale electrophysiological and imaging approaches continue to expand [46,56], it will be important to assess whether these principles generalize to more heterogeneous networks. Prior work suggests that distance from criticality may vary hierarchically across brain areas [11,57–60], raising the possibility that different regions contribute differently to multiscale coordination.

However, it is still unclear whether these variations reflect local properties or emerge from dynamic interactions across the connectome. Large-scale computational models have begun to address these questions, linking local to global brain dynamics. In particular, the accompanying paper [60] introduces a multiscale model displaying the coemergence of local and global near-critical dynamics, and provides the first *in silico* evidence that local distance from criticality is shaped both by the local properties and by the long-range interactions over the connectome. Future work exploring how critical dynamics develop on multiple scales may reveal their role in supporting flexible computations and how they relate to neurological and psychiatric (dys)function [53,61–65].

IV. METHODS

A. Data acquisition and processing

Recordings from three male Long-Evans rats (350–400 g at the time of surgery) were used for this study. All data in this stud y came from a previously published study [66]. Full details about animal care, surgery, data acquisition, and processing can be found in [66,67]. In compliance with European Directives 86/609/CEE and 2010/63/UE, all experiments were evaluated by an ethics committee (CEEA No. 59) and approved by the French Ministry of Research (authorization No. 8229).

Briefly, the animals were housed individually in monitored conditions (21 °C and 45% humidity) and maintained on a 12 h light –12 h dark cycle. To avoid obesity, food was restricted to 13 − 16 g of rat chow per day, while water was available *ad libitum*. To habituate the rats to human manipulation, they were handled each workday. Then 16–24 bundles of twisted-wire electrodes were implanted in the PFC 2.5–4.8 mm anterior and ±0.3–0.6 mm lateral from bregma with reference and ground screws in the cerebellum. Brain activity was recorded with a 256-channel digital data acquisition system (KJE-1001, Amplipex, Szeged, Hungary).

The animals underwent a multiday habituation, fear conditioning, and recall test protocol as described in [67], and the two sessions per animal used here correspond to the habituation and conditioning phases. The signals were continuously acquired over ∼8 h per session with four 64-channel headstages (Amplipex HS2) and sampled in wideband at 20 kHz. An inertial measurement unit sampled the three-dimensional (3D) angular velocity and linear acceleration of the head at 300 Hz. Off-line spike sorting was performed using KiloSort 1.0 [68]. The resulting clusters were visually inspected, using KLUSTERS [69], to reject noise and to merge units erroneously considered as different units. The total number of single units registered in the right (left) hemisphere of the three animals was: 127 (133), 78 (129), and 81 (72).

B. Time window segmentation

Continuous spiking data from each PFC population were divided into nonoverlapping 5-s segments to capture temporal fluctuations in population activity, unless otherwise stated. Each 5-s window was treated independently for subsequent analyses, including the computation of mean pairwise spiking correlations and neuronal avalanches. This segmentation allowed us to examine dynamic changes in synchrony and criticality over time while maintaining sufficient temporal resolution to detect avalanches.

C. Pairwise spike correlations

To compute pairwise spike-train correlations ρ, spike trains $s(t)$ were discretized using fixed 20-ms time bins and then convolved with a kernel k:

$$s^c(t) = k(t)s(t), \tag{1}$$

where k is a Mexican hat kernel defined as the difference between two zero-mean Gaussian distributions with standard deviations of 100 and 400 ms, respectively [16,39–70]. From the convolved spike trains, $s^c(t)$, we computed the pairwise correlation between units i and j as

$$\rho_{i,j} = \frac{\mathrm{Cov}\left(s_i^c, s_j^c\right)}{\sqrt{\mathrm{Var}\left(s_j^c\right)\mathrm{Var}\left(s_i^c\right)}}, \tag{2}$$

where Cov denotes covariance and Var denotes variance. The mean pairwise correlation, $\langle\rho\rangle$, was used as a measure of population-level synchrony.

D. Neuronal avalanches analysis

Spiking activity from simultaneously recorded neurons was binned in time using a bin width ΔT defined as the mean interspike interval of the pooled population activity; that is, the merged spike train across all neurons in the population under consideration [16]. This procedure was applied separately to the left PFC, right PFC, and merged L + R populations. Avalanche detection was performed independently within each 5-s segment, with ΔT recomputed from the corresponding pooled population activity. In this framework, ΔT reflects a state-dependent population timescale rather than a globally fixed bin width or the mean of individual-neuron interspike intervals, following the rationale used in previous work [25].

An avalanche was defined as a sequence of consecutive time bins containing at least one spike, bounded before and after by empty bins [6]. The size of an avalanche, S, was calculated as the total number of spikes occurring across all occupied bins in the event. The duration, T, was defined as the number of consecutive occupied bins. Avalanches were then grouped according to synchrony level using 30 nonoverlapping bins spanning the full observed range of $\langle\rho\rangle(t)$. To fit the power-law distributions of avalanche sizes $P(S) \sim S^{-\tau}$ and durations $P(T) \sim T^{-\tau_t}$, and to obtain their corresponding critical exponents, a maximum likelihood estimator was used [16,71]. For avalanche size (duration), the lower $x_{\min} = 3(2)$ and upper $x_{\max} = 35(18)$ bounds of the fitting range were defined independently, and the corresponding power-law fits were restricted to observations within these bounds.

To compare the relative support for the power-law and log-normal models, we computed the Akaike information criterion [72], $\mathrm{AIC} = 2k - 2\ln(\hat{L}) + (2k^2 + 2k)/(N - k - 1)$, for each fitted distribution, where $\hat{L}$ is the maximized log-likelihood obtained from maximum likelihood estimation over the same truncated range $[x_{\min}, x_{\max}]$, k is the number of free parameters, and N is the sample size. The power-law model has one free parameter ($k = 1$), the scaling exponent τ, since $x_{\min}$ and $x_{\max}$ were fixed rather than estimated. The log-normal model has two free parameters ($k = 2$), the mean μ, and standard deviation σ of $\ln(x)$. As in [16], we then defined $\Delta_{\mathrm{AIC}} = \mathrm{AIC}_{\mathrm{LN}} - \mathrm{AIC}_{\mathrm{PL}}$, such that $\Delta_{\mathrm{AIC}} > 0$ indicates the power-law model fits the data better than the log-normal, and $\Delta_{\mathrm{AIC}} < 0$ indicates the reverse.

As a stringent test of critical dynamics, the scaling relation between avalanche size and duration, $\langle S\rangle(T) \sim T^{1/\sigma\nu z}$, was compared with the expected relation $\frac{1}{\sigma\nu z} = \frac{\tau_t - 1}{\tau - 1}$ [19]. The absolute difference between these two quantities was defined as the "distance to criticality coefficient" (DCC) [21]. DCC was computed for each segment and assessed across the observed range of population synchrony, characterizing the

system's proximity to a critical point. For SM Fig. S4 only [17], occupancy bins were defined using a DCC threshold, set to the median of its distribution. Moreover, to formally test for a U-shaped relationship between DCC and synchrony, we applied the test for a U-shaped relationship [20], which evaluates whether the slope of a fitted quadratic curve is significantly negative at the lower bound and significantly positive at the upper bound of the observed range. This provides an exact test for the presence of a U-shaped relationship, rather than a simple test of curvature.

E. Null models and partition controls

We used complementary null models and partition controls to assess whether the observed coordination between left and right PFC populations could be explained by chance temporal alignment, local coactivation structure, or arbitrary partitioning of the recorded neurons.

First, to test whether the apparent coordination between the synchrony levels of the two hemispheres could arise by chance, we generated surrogate datasets by shuffling the right-hemisphere synchrony time series, $\langle \rho_R \rangle(t)$, across nonoverlapping 5-s windows. This procedure preserved the distribution of intrahemispheric synchrony values within each hemisphere while disrupting their temporal alignment across hemispheres. For each surrogate, we recomputed the occupancy probabilities across the 3×3 synchronization-state space defined by the left and right population synchrony levels. The empirical occupancy probability, P_{data}, in each bin was then compared with the corresponding surrogate distribution, P_{null}, obtained from 1000 shuffled datasets. Statistical significance was assessed using an empirical two-tailed permutation test: for each bin, the empirical deviation from the null mean was compared with the distribution of absolute deviations obtained from the shuffled surrogates. Significance was defined as $\alpha < 0.05$. These analyses are presented in SM Fig. S5 [17].

Second, to test whether the relationship between intrahemispheric synchrony and interhemispheric correlation could be explained by preserved local coactivation structure alone, we constructed an epochwise temporal-shuffling null model. For each 5-s epoch, the spiking activity of each hemisphere was represented as a matrix of neurons by time bins. We then randomly permuted the time bins of this matrix independently for the two hemispheres. Because the permutation was applied to the entire time columns, the instantaneous correlation structure among neurons within each hemisphere was preserved, while temporal alignment between hemispheres was disrupted. We then recomputed the mean interhemispheric correlation, excluding intrahemispheric pairs, and repeated the gradient analysis relating interhemispheric correlation to the mean intrahemispheric synchrony of the two populations. Slopes were estimated using linear regression and compared with the distribution of slopes obtained from 1000 surrogate datasets. These analyses are presented in Fig. 3.

To determine whether the observed effects were specific to the anatomical left-right organization, rather than a generic consequence of splitting a correlated population, we performed random partition controls. For each recording session, neurons from the left and right PFC were pooled and randomly reassigned into two virtual populations matched in size to the empirical left and right PFC populations. This procedure was repeated 100 times per session. For each random partition, we repeated the same analysis pipeline used for the empirical hemispheric split. Moreover, we compared the dispersion of the synchrony scatter around the identity line and the slope of the interpopulation correlation gradient between empirical and randomly partitioned populations. The empirical p-value was obtained by calculating the fraction of null permutations whose metric value exceeded the empirical observation (one-tailed). These analyses are presented in SM Fig. S8 [17].

Finally, to test whether the interpopulation gradient could arise from shared local state fluctuations within a single hemisphere, we performed a within-hemisphere virtual-partition control. For each session, neurons from one hemisphere were randomly divided into two size-matched virtual populations, and the same intra- and interhemispheric correlation analyses were repeated. To ensure a matched comparison, we also generated a size-matched empirical distribution by repeatedly subsampling neurons from the real left and right PFC populations and recomputing the left-right gradient. The slope distributions obtained from the within-hemisphere virtual partitions and the size-matched empirical left-right partitions were compared using a two-sided Mann-Whitney U test. These analyses are presented in SM Fig. S9 [17].

V. COMPUTATIONAL MODEL

A. Local model

Each cortical region was modeled as a network of K all-to-all coupled active rotators of the Shinomoto-Kuramoto type, the system whose hybrid-type synchronization transition produces scale-free neuronal avalanches [41]. The phase φ_i of unit i in region n obeys

$$\dot{\varphi}_{i,n} = \omega + a_n \sin\varphi_{i,n} + \frac{J}{K}\sum_j \sin(\varphi_{j,n} - \varphi_{i,n}) + I_{i,n}(t) + \sigma\,\eta_{i,n}(t), \tag{3}$$

where ω is the intrinsic frequency, J the within-region coupling, a_n the excitability, and $\eta_{i,n}$ is zero-mean unit-variance Gaussian white noise of amplitude σ. We fixed $\omega = J = 1$ and $\sigma = 0.499$ and used a as the control parameter. A spike was defined as an upward crossing of $\sin\varphi_{i,n}$ through the threshold $y_{\text{th}} = 0.6$. The single isolated unit undergoes a saddle node on invariant circle bifurcation at $a = \omega$; in the finite network, the collective synchronization transition sits at $a_{\text{crit}} \approx 1.07$, where the firing rate collapses.

B. Coupled regions and drives

For the two-region simulations we coupled populations through $I_{i,n}(t)$ and, where indicated, a shared external input representing afferents from the rest of the brain:

$$I_{i,n}(t) = \frac{G}{K}\sum_{m\neq n}\sum_{j\in m} A_{ij}^{nm}\,\sin(\varphi_{j,m} - \varphi_{i,n}) + g_{\text{in}}\,F(t)\,\sin[\theta(t) - \varphi_{i,n}]. \tag{4}$$

TABLE I. Model and analysis parameters.

Symbol	Meaning	Value
	Local model	
ω	Intrinsic frequency	1
J	Within-region coupling	1
σ	Noise amplitude	0.499
a	Excitability (control parameter)	Swept; $a_{\text{crit}} \approx 1.07$
K	Units per population	250 (5000 for avalanche or criticality)
y_{th}	Spike threshold on $\sin\varphi$	0.6
$\mathrm{d}t$	Integration step	0.01 (0.005 at $K = 5000$)
	Inter-regional coupling	
G	Interregional coupling	0.3 (swept 0–0.8)
A^{nm}	Between-region graph	Sparse $p_{\text{between}} = 0.2$
	Slow drives (dynamic regime, Fig. 5)	
τ_a	Excitability correlation time	6 s
s_a	Excitability std	0.06
a_{corr}	Interpopulation drive correlation	0.7
g_{in}	Common-input global scale	0.2
τ_{in}	Common-input correlation time	6 s
	Observables	
$\langle\rho\rangle$	Synchrony (pairwise spike correlation)	10 ms bins
χ	Criticality susceptibility	Fano factor (variance or mean) of activity
ΔT	Avalanche bin	Mean interevent interval
–	Units subsampled for avalanches/$\langle\rho\rangle$	∼300

G scales the inter-regional coupling. The between-region connectivity A^{nm} was a sparse random graph of density $p_{\text{between}} = 0.2$, whereas within-region connectivity was always all to all. The shared input had a global scale g_{in} and a slowly varying strength $F(t)$. To let the model fluctuate around criticality, the excitabilities drift as an Ornstein-Uhlenbeck process centered on a_{crit} with a stationary standard deviation s_a and correlation time τ_a; the two populations' drives shared a common component, giving them a correlation a_{corr}.

C. Numerical methods and data analysis

Population synchrony was defined as the mean pairwise correlation $\langle\rho\rangle$ of the spike trains, binned at 10 ms, with correlations computed as described in Eq. (2). The Kuramoto modulus $R = |Z|$ remains a useful descriptor of phase coherence, but it is not a reliable *criticality* indicator for inhomogeneous active rotators: $|Z|$ stays large even in the asynchronous regime, because units dwell unevenly across phases, so $\mathrm{Var}(R)$ peaks away from the transition. As the criticality susceptibility, we therefore used the Fano factor (variance over mean) of the population activity, the avalanche or branching susceptibility, which is maximal at the synchronization transition [Fig. 4(b)]; it peaks at $a_{\text{crit}} \approx 1.07$, coincident with the $\langle\rho\rangle$ collapse, whereas $\mathrm{Var}(R)$ spuriously peaks earlier.

The computational model was simulated with the Euler-Maruyama scheme at step $\mathrm{d}t$. One second of simulation time was interpreted as one real millisecond, which set realistic unit firing rates; correlation times reported in seconds use this factor. All simulations used a custom `numba`-compiled integrator; parameters are listed in Table I.

ACKNOWLEDGMENTS

L.D.P. acknowledges support from the European Union (ERC, NEMESIS, Project No. 101071900), AGAUR cofunded by the Departament de Recerca i Universitats de la Generalitat de Catalunya (AGAUR Grant No. 2021-SGR-01165), and the Brazilian agency CNPq (Grant No. 444500/2024-3). G.R. acknowledges support from the Marie Skłódowska-Curie Postdoctoral Fellowship (Project CAERUS) under the European Union's Horizon Europe research and innovation program (Grant No. 101199894).

L.D.P. and G.R. designed the research; G.R. and P.B. performed simulations; M.N.P. performed experiments and preprocessed experimental data; L.D.P., P.B., and G.R. analyzed the data; L.D.P. and G.R. organized the results; L.D.P. wrote the first draft; all authors discussed the results and wrote the paper.

DATA AVAILABILITY

The code supporting the findings of this study is publicly available at the GitHub repository [73]. The data supporting the findings of this study are available from the corresponding author upon reasonable request.

[1] G. Tononi, O. Sporns, and G. M. Edelman, A measure for brain complexity: Relating functional segregation and integration in the nervous system., Proc. Natl. Acad. Sci. USA **91**, 5033 (1994).

[2] J. R. Cohen and M. D'Esposito, The segregation and integration of distinct brain networks and their relationship to cognition, J. Neurosci. **36**, 12083 (2016).

[3] M. C. Rosen and D. J. Freedman, How distributed is the brain-wide network that is recruited for cognition? Nat. Rev. Neurosci. **27**, 138 (2025).

[4] A. Zalesky, A. Fornito, L. Cocchi, L. L. Gollo, and M. Breakspear, Time-resolved resting-state brain networks, Proc. Natl. Acad. Sci. USA **111**, 10341 (2014).

[5] J. M. Beggs, The criticality hypothesis: How local cortical networks might optimize information processing, Philos. Trans. R. Soc. A **366**, 329 (2008).

[6] J. M. Beggs and D. Plenz, Neuronal avalanches in neocortical circuits, J. Neurosci. **23**, 11167 (2003).

[7] J. M. Palva and S. Palva, The correlation of the neuronal long-range temporal correlations, avalanche dynamics with the behavioral scaling laws and interindividual variability, in *Criticality in Neural Systems*, edited by D. Plenz and E. Niebur (Wiley, Hoboken, NJ, 2014) .

[8] W. L. Shew and D. Plenz, The functional benefits of criticality in the cortex, Neuroscientist **19**, 88 (2013).

[9] K. B. Hengen and W. L. Shew, Is criticality a unified setpoint of brain function? Neuron **113**, 2582 (2025).

[10] S. A. Jones, J. H. Barfield, V. K. Norman, and W. L. Shew, Scale-free behavioral dynamics directly linked with scale-free cortical dynamics, eLife **12**, e79950 (2023).

[11] B. Harris, L. L. Gollo, and B. D. Fulcher, Tracking the distance to criticality in systems with unknown noise, Phys. Rev. X **14**, 031021 (2024).

[12] A. J. Fontenele, J. S. Sooter, V. K. Norman, S. H. Gautam, and W. L. Shew, Low-dimensional criticality embedded in high-dimensional awake brain dynamics, Sci. Adv. **10**, eadj9303 (2024).

[13] D. Dahmen, S. Grün, M. Diesmann, and M. Helias, Second type of criticality in the brain uncovers rich multiple-neuron dynamics, Proc. Natl. Acad. Sci. USA **116**, 13051 (2019).

[14] J. S. Sooter, A. J. Fontenele, A. K. Barreiro, C. Ly, K. B. Hengen, and W. L. Shew, Defining and measuring proximity to criticality, bioRxiv (2025).

[15] G. Hahn, A. Ponce-Alvarez, C. Monier, G. Benvenuti, A. Kumar, F. Chavane, G. Deco, and Y. Frégnac, Spontaneous cortical activity is transiently poised close to criticality, PLoS Comput. Biol. **13**, e1005543 (2017).

[16] A. J. Fontenele, N. A. de Vasconcelos, T. Feliciano, L. A . A. Aguiar, C. Soares-Cunha, B. Coimbra, L. Dalla Porta, S. Ribeiro, A. J. Rodrigues, N. Sousa, *et al.*, Criticality between cortical states, Phys. Rev. Lett. **122**, 208101 (2019).

[17] See Supplemental Material at http://link.aps.org/supplemental/10.1103/tr2q-757y for (Fig. S3) a comparison between log-normal and power-law goodness of fit for size and duration of neuronal avalanches across synchrony levels; (Figs. S1 and S2) an analysis of avalanche size across animals, hemispheres, and recording sessions; (Fig. S4) the distance to criticality analysis using a time window of 10 s for defining the population synchrony level; (Fig. S5) the surrogate-data testing to assess whether the observed co-occurrence of synchronization states exceeds chance levels; (Fig. S6) analyis of the intrahemispheric correlation gradient across animals, hemispheres, and recording sessions; (Fig. S7) a comparison between empirical and random partition control avalanche distributions for size and duration at intermediate synchrony levels; (Fig. S8) the statistical analysis of the interhemispheric correlation structure, quantified by orthogonal dispersion and gradient slope, comparing the empirical structure with random partition controls; (Fig. S9) the statistical analysis of the interhemispheric correlation structure, quantified by the gradient slope, compared with a null distribution derived from virtual partitions of a single hemisphere; (Fig. S10) the computational model analysis of the interpopulation gradient in two uncoupled populations.

[18] M. A. Muñoz, R. Dickman, A. Vespignani, and S. Zapperi, Avalanche and spreading exponents in systems with absorbing states, Phys. Rev. E **59**, 6175 (1999).

[19] N. Friedman, S. Ito, B. A. W. Brinkman, M. Shimono, R. E. Lee DeVille, K. A. Dahmen, J. M. Beggs, and T. C. Butler, Universal critical dynamics in high resolution neuronal avalanche data, Phys. Rev. Lett. **108**, 208102 (2012).

[20] J. T. Lind and H. Mehlum, With or without U? The appropriate test for a U-shaped relationship, Oxford Bull. Econ. Stat. **72**, 109 (2010).

[21] Z. Ma, G. G. Turrigiano, R. Wessel, and K. B. Hengen, Cortical circuit dynamics are homeostatically tuned to criticality invivo, Neuron **104**, 655 (2019).

[22] Y. Xu, A. Schneider, R. Wessel, and K. B. Hengen, Sleep restores an optimal computational regime in cortical networks, Nat. Neurosci. **27**, 328 (2024).

[23] J. O'Byrne and K. Jerbi, How critical is brain criticality? Trends Neurosci. **45**, 820 (2022).

[24] S. di Santo, P. Villegas, R. Burioni, and M. A. Muñoz, Landau–Ginzburg theory of cortex dynamics: Scale-free avalanches emerge at the edge of synchronization, Proc. Natl. Acad. Sci. USA **115**, E1356 (2018).

[25] S. Yu, T. L. Ribeiro, C. Meisel, S. Chou, A. Mitz, R. Saunders, and D. Plenz, Maintained avalanche dynamics during task-induced changes of neuronal activity in nonhuman primates, eLife **6**, e27119 (2017).

[26] M. A. Muñoz, *Colloquium*: Criticality and dynamical scaling in living systems, Rev. Mod. Phys. **90**, 031001 (2018).

[27] J. P. Sethna, K. A. Dahmen, and C. R. Myers, Crackling noise, Nature (London) **410**, 242 (2001).

[28] S.-S. Poil, R. Hardstone, H. D. Mansvelder, and K. Linkenkaer-Hansen, Critical-state dynamics of avalanches and oscillations jointly emerge from balanced excitation/inhibition in neuronal networks, J. Neurosci. **32**, 9817 (2012).

[29] L. Dalla Porta and M. Copelli, Modeling neuronal avalanches and long-range temporal correlations at the emergence of collective oscillations: Continuously varying exponents mimic M/EEG results, PLoS Comput. Biol. **15**, e1006924 (2019).

[30] L. Nowak, M. Munk, J. Nelson, A. James, and J. Bullier, Structural basis of cortical synchronization. I. Three types of interhemispheric coupling, J. Neurophysiol. **74**, 2379 (1995).

[31] X. Yin, Y. Wang, J. Li, and Z. V. Guo, Lateralization of short-term memory in the frontal cortex, Cell Rep. **40**, 111190 (2022).

[32] S. L. Brincat, J. A. Donoghue, M. K. Mahnke, S. Kornblith, M. Lundqvist, and E. K. Miller, Interhemispheric transfer of working memories, Neuron **109**, 1055 (2021).

[33] M. Ghosh, F.-C. Yang, S. P. Rice, V. Hetrick, A. L. Gonzalez, D. Siu, E. K. Brennan, T. T. John, A. M. Ahrens, and O. J. Ahmed, Running speed and REM sleep control two distinct modes of rapid interhemispheric communication, Cell Rep. **40** 111028 (2022).

[34] O. Sporns, The human connectome: A complex network, Ann. NY Acad. Sci. **1224**, 109 (2011).

[35] R. F. Betzel and D. S. Bassett, Specificity and robustness of long-distance connections in weighted, interareal connectomes, Proc. Natl. Acad. Sci. USA **115**, E4880 (2018).

[36] B. A. Sauerbrei, J.-Z. Guo, J. D. Cohen, M. Mischiati, W. Guo, M. Kabra, N. Verma, B. Mensh, K. Branson, and A. W. Hantman, Cortical pattern generation during dexterous movement is input-driven, Nature (London) **577**, 386 (2020).

[37] T. A. Machado, I. V. Kauvar, and K. Deisseroth, Multiregion neuronal activity: The forest and the trees, Nat. Rev. Neurosci. **23**, 683 (2022).

[38] A. K. Engel, P. König, A. K. Kreiter, and W. Singer, Interhemispheric synchronization of oscillatory neuronal responses in cat visual cortex, Science **252**, 1177 (1991).

[39] P. Sorrentino, C. Seguin, R. Rucco, M. Liparoti, E. Troisi Lopez, S. Bonavita, M. Quarantelli, G. Sorrentino, V. Jirsa, and A. Zalesky, The structural connectome constrains fast brain dynamics, eLife **10**, e67400 (2021).

[40] G. Deco, G. Tononi, M. Boly, and M. L. Kringelbach, Rethinking segregation and integration: Contributions of whole-brain modelling, Nat. Rev. Neurosci. **16**, 430 (2015).

[41] V. Buendía, P. Villegas, R. Burioni, and M. A. Muñoz, Hybrid-type synchronization transitions: Where incipient oscillations, scale-free avalanches, and bistability live together, Phys. Rev. Res. **3**, 023224 (2021).

[42] S. Shinomoto and Y. Kuramoto, Phase transitions in active rotator systems, Prog. Theor. Phys. **75**, 1105 (1986).

[43] D. Toker, I. Pappas, J. D. Lendner, J. Frohlich, D. M. Mateos, S. Muthukumaraswamy, R. Carhart-Harris, M. Paff, P. M. Vespa, M. M. Monti, F. T. Sommer, R. T. Knight, and M. D'Esposito, Consciousness is supported by near-critical slow cortical electrodynamics, Proc. Natl. Acad. Sci. USA **119**, e2024455119 (2022).

[44] D. M. Castro, T. Feliciano, N. A. P. de Vasconcelos, C. Soares-Cunha, B. Coimbra, A. J. Rodrigues, P. V. Carelli, and M. Copelli, In and out of criticality? State-dependent scaling in the rat visual cortex, PRX Life **2**, 023008 (2024).

[45] T. A. Engel and N. A. Steinmetz, New perspectives on dimensionality and variability from large-scale cortical dynamics, Curr. Opin. Neurobiol. **58**, 181 (2019).

[46] C. Stringer, M. Pachitariu, N. Steinmetz, C. B. Reddy, M. Carandini, and K. D. Harris, Spontaneous behaviors drive multidimensional, brainwide activity, Science **364**, eaav7893 (2019).

[47] R. V. Raut, Z. P. Rosenthal, X. Wang, H. Miao, Z. Zhang, J.-M. Lee, M. E. Raichle, A. Q. Bauer, S. L. Brunton, B. W. Brunton, and J. Nathan Kutz, Arousal as a universal embedding for spatiotemporal brain dynamics, Nature (London) **647**, 454 (2025).

[48] S. Musall, M. T. Kaufman, A. L. Juavinett, S. Gluf, and A. K. Churchland, Single-trial neural dynamics are dominated by richly varied movements, Nat. Neurosci. **22**, 1677 (2019).

[49] B. R. Munn, C. Whyte, E. J. Müller, and J. M. Shine, Arousal tunes neuronal avalanches across a directed percolation critical point, Phys. Rev. E **114**, 024403 (2026).

[50] Y. Oran, Y. Katz, M. Sokoletsky, K. C.-K. Malina, and I. Lampl, Reduction of corpus callosum activity during whisking leads to interhemispheric decorrelation, Nat. Commun. **12**, 4095 (2021).

[51] C. J. Honey, R. Kötter, M. Breakspear, and O. Sporns, Network structure of cerebral cortex shapes functional connectivity on multiple time scales, Proc. Natl. Acad. Sci. USA **104**, 10240 (2007).

[52] L. Dalla Porta, J. Fousek, A. Destexhe, and M. V. Sanchez-Vives, Spatially structured heterogeneity shapes large-scale cortical dynamics in a model of the human cortex, Proc. Natl. Acad. Sci. USA **123**, e2532072123 (2026).

[53] L. Cocchi, L. L. Gollo, A. Zalesky, and M. Breakspear, Criticality in the brain: A synthesis of neurobiology, models and cognition, Prog. Neurobiol. **158**, 132 (2017).

[54] O. Sporns, Network attributes for segregation and integration in the human brain, Curr. Opin. Neurobiol. **23**, 162 (2013).

[55] S. Bhattacharya, S. L. Brincat, M. Lundqvist, and E. K. Miller, Traveling waves in the prefrontal cortex during working memory, PLoS Comput. Biol. **18**, e1009827 (2022).

[56] C. Findling, F. Hubert, L. Acerbi, B. Benson, J. Benson, D. Birman, N. Bonacchi, E. K. Buchanan, S. Bruijns, M. Carandini, J. A. Catarino, G. A. Chapuis, A. K. Churchland, Y. Dan, F. Davatolhagh, E. E. J. DeWitt, T. A. Engel, M. Fabbri, M. A. Faulkner, I. R. Fiete, *et al.*, Brain-wide representations of prior information in mouse decision-making, Nature (London) **645**, 192 (2025).

[57] G. B. Morales, S. di Santo, and M. A. Muñoz, Quasiuniversal scaling in mouse-brain neuronal activity stems from edge-of-instability critical dynamics, Proc. Natl. Acad. Sci. USA **120**, e2208998120 (2023).

[58] G. G. Cambrainha, D. M. Castro, L. L. Gollo, P. V. Carelli, and M. Copelli, Hierarchical organization of critical brain dynamics, arXiv:2604.21832.

[59] D. Yellin, E. Simony, R. Malach, and O. Shriki, A cortical gradient of distance to criticality governs large-scale resting-state fMRI dynamics, bioRxiv (2026).

[60] G. Rabuffo, P. Bozzo, B. Nguyen, D. Depannemaecker, M. N. Pompili, L. L. Gollo, T. Fukai, P. Sorrentino, and L. Dalla Porta, companion paper, Connectome modulates critical brain dynamics across local and global scales, Phys. Rev. Res. **8**, 043168 (2026).

[61] V. Zimmern, Why brain criticality is clinically relevant: A scoping review, Front. Neural Circuits **14**, 54 (2020).

[62] P. M. Müller, G. Miron, M. Holtkamp, and C. Meisel, Critical dynamics predicts cognitive performance and provides a common framework for heterogeneous mechanisms impacting cognition, Proc. Natl. Acad. Sci. USA **122**, e2417117122 (2025).

[63] Y. Xin, Y. Cui, S. Yu, and N. Liu, Genetic contributions to brain criticality and its relationship with human cognitive functions, Proc. Natl. Acad. Sci. USA **122**, e2417010122 (2025).

[64] D. Newman, C. Maschke, J. O'Byrne, M. A. Colombo, A. Comanducci, S. Casarotto, G. Citerio, M. Rosanova, M. Massimini, K. Jerbi, *et al.*, Critical dynamics in spontaneous EEG predict perturbational complexity in disorders of consciousness with measurable evoked responses, bioRxiv (2026).

[65] G. G. Cambrainha, D. M. Castro, N. A. P. de Vasconcelos, P. V. Carelli, and M. Copelli, Criticality at work: Scaling in the mouse cortex enhances performance, PRX Life **3**, 033026 (2025).

[66] M. N. Pompili, R. Todorova, C. J. Boucly, E. M. Leroux, S. I. Wiener, and M. Zugaro, Adaptive communication between cell assemblies and "reader" neurons shapes flexible brain dynamics, PLoS Biol. **23**, e3003505 (2025).

[67] M. N. Pompili, N. Hamou, and S. I. Wiener, Integration of fear learning and fear expression across the dorsoventral axis of the hippocampus, Proc. Natl. Acad. Sci. USA **123**, e2520207123 (2026).

[68] M. Pachitariu, N. A. Steinmetz, S. N. Kadir, M. Carandini, and K. D. Harris, Fast and accurate spike sorting of high-channel count probes with KiloSort, in *Advances in Neural Information Processing Systems*, Vol. 29, edited by D. Lee, M. Sugiyama, U. Luxburg, I. Guyon, and R. Garnett (Curran Associates, Inc., Red Hook, NY, 2016).

[69] L. Hazan, M. Zugaro, and G. Buzsáki, Klusters, NeuroScope, NDManager: A free software suite for neurophysiological data processing and visualization, J. Neurosci. Methods **155**, 207 (2006).

[70] A. Renart, J. de la Rocha, P. Bartho, L. Hollender, N. Parga, A. Reyes, and K. D. Harris, The asynchronous state in cortical circuits, Science **327**, 587 (2010).

[71] J. Alstott, E. Bullmore, and D. Plenz, Powerlaw: A Python package for analysis of heavy-tailed distributions, PLoS One **9**, e85777 (2014).

[72] H. Akaike, A new look at the statistical model identification, IEEE Trans. Autom. Control **19**, 716 (1974).

[73] L. Dalla Porta, Code for intra- and interhemispheric criticality, Github repository 2026, https://github.com/ldallap/intra-interhemispheric-criticality.